Planar and fibre textures induced in isotactic polypropylene on equibiaxial hydrostatic deformation

R. F. Saraf
T. J. Watson Research Center, IBM Corporation, Yorktown Heights, NY 10598, USA
(Received 7 April 1993; revised 28 June 1993)

Wide-angle X-ray scattering studies on equibiaxially deformed isotactic polypropylene (i-PP) have been carried out. The equibiaxial deformation is achieved by uniaxial compression below the melting point at 60 and 140°C. The study proves the equibiaxiality of the deformation with the observation of two types of crystal textures referred to as planar and fibrillar. These textures are quantified by relating the intensity distribution for a (110) reflection to the orientation distribution of the crystals. The signature of the fibre-like texture in the intensity distribution (of a given (*hkl*) reflection) is obvious; the manifestation of the planar texture requires a closer analysis of the pole figure. An 'exact method' of formulation is used to estimate the relative fractions of the two textures. The quantitative change in the relative fraction as a function of compression ratio is explained in terms of a qualitative model based on slip systems. The mechanism of the texture developed in i-PP as a function of compression ratio is discussed in the light of crystal slip systems and the order–disorder transition during the deformation process. The latter phenomenon is shown to be a favourable route to obtaining a high chain orientation and a larger amount of the planar texture relative to the fibrillar texture.

(Keywords: isotactic polypropylene; equibiaxial deformation; wide-angle X-ray scattering)

INTRODUCTION

It is well known that the mechanical properties, i.e. tensile modulus and strength, of semicrystalline polymers strongly depend on the crystal content and its orientation[1,2]. One commonly used method to induce crystal texture is deformation of the polymer below its melting point. In the simplest solid-forming processes involving uniaxial stretching, the chains orient parallel to the draw direction, thus enhancing the modulus in that direction[3]. The uniaxial extension is significantly modified when deformation is carried out under high hydrostatic pressure, which tends to increase the elongational viscosity and consequently increase the relaxation time of the stretched chain as it undergoes deformation[4–6]. The result is a high draw efficiency of the chain[7].

The deformation mechanism to achieve chain orientation is explained accurately in terms of lamellae shearing parallel to the chain axis followed by a pulling-out of the chains to form extended fibrillation[3,8]. This mechanism, suggested by Peterlin, is proved by direct observation of the deformation process using transmission electron microscopy for a variety of semicrystalline polymers[9–20]. To achieve high modulus and tensile strength, the bridges between the pulled out, extended molecules are formed by recrystallization of unstretched chains. Therefore, if the entanglement density can be reduced in a high-molecular-weight polymer, high deformation should lead to complete transformation from a lamellar to a fibrillar structure where the chain ends and folds are incorporated to form a continuous crystal[21]. One approach to reducing the entanglement density in high-molecular-weight polymers and hence achieving high draw ratios is the slow recrystallization of the polymer from dilute solution to form single-crystal mats. In a remarkable set of experiments involving hydrostatic deformation followed by uniaxial stretching of single-crystal mats, Kanamoto *et al.*[22,23] have achieved ultrahigh draw ratios of 300× and 65× for ultrahigh-molecular-weight polyethylene and polypropylene, with moduli of 222 and 33 GPa, respectively. Since the moduli of the crystals along the chain axis as measured by X-ray diffraction are 240 and 42 GPa for polyethylene and polypropylene, respectively, the obtained structure is close to a continuous crystal morphology[24].

The large uniaxial chain orientation, however, causes a concomitant decrease in the tensile modulus and strength in the lateral direction. Furthermore, since the chains (especially in the case of polyolefins) are held together by weak van der Waals forces, they tend to slip past each other and cause significant creep. To overcome these deficiencies, multiaxial strain processes such as biaxial deformation are performed. Although the maximum modulus achieved is lower compared to uniaxial deformation, creep reduction and an enhancement of properties in two directions are achieved.

In this paper, we describe the quantitative measurement of the orientation distribution of the chain axis resulting from the simultaneous equibiaxial deformation of isotactic polypropylene (i-PP). The deformation strain field was achieved by uniaxial compression along the

0032-3861/94/07/1359–10

thickness direction (z axis) to achieve simultaneous deformation in the radial (r axis) and tangential (θ axis) directions. The biaxial deformation field due to uniaxial compression has the following advantages over other geometries such as tenterframing[25], tubular extrusion[26] and blowing[27]: (i) the strain field is equibiaxial[28]; (ii) there is a uniform strain field over the sample[28]; (iii) there is a large hydrostatic pressure during deformation[28]; and (iv) the strain rate increases with time, in contrast to other biaxial stretching processes[29]. We first briefly describe the method of obtaining the equibiaxial deformation strain field, and then give a qualitative description of the expected crystal texture. We then develop a formulation to quantify and interpret the various textures measured by X-ray diffraction. We finally discuss the deformation mechanism and the role of the order–disorder phase transition that occurs during compression. It will become apparent that the biaxial deformation field reveals more specific and quantitative information on the formation and role of the disordered phase than the uniaxial deformation field[30–33].

EXPERIMENTAL

Isotactic polypropylene (i-PP) of molecular weight $\sim 2.9 \times 10^5$ and polydispersity ~ 2 was moulded into a roughly 5.6 mm thick sheet. The moulding was done under vacuum (~ 0.1 mmHg), to avoid degradation and air bubbles, at a temperature of 220°C. The mould was subsequently quenched in iced water to yield a white, opaque, semicrystalline i-PP sheet. Wide-angle X-ray scattering (WAXS) indicated that the crystal modification was all monoclinic (i.e. the α form), as shown by the sharp (110) and (040) peaks in *Figure 1*. The (111) and (041) peaks of the as-moulded sample (*Figure 1*) are better resolved after annealing at 160°C (*Figure 2*). The crystal forms in *Figures 1* and *2* are thus $\alpha 1$ and $\alpha 2$, respectively[34]. Furthermore, the invariance in the relative intensities of the various peaks on tilting the sample implies an isotropic orientation. The heat of fusion measured on a Perkin–Elmer DSC-2 was ~ 22.1 cal g^{-1} (1 cal = 4.2 J), corresponding to $\sim 50\%$ crystallinity.

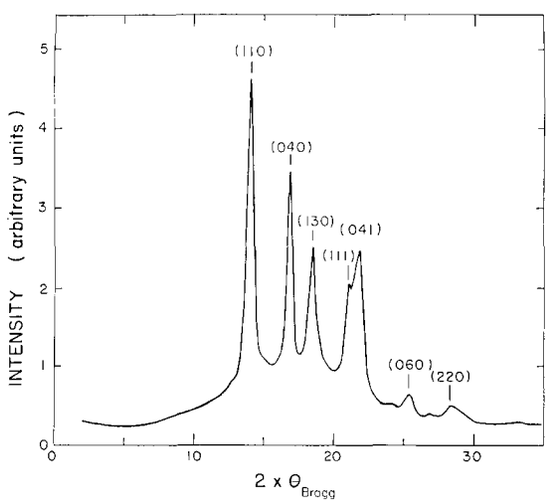

Figure 1 The WAXS scan of as-moulded i-PP sheet. The relative intensities of the various peaks indicate a powder pattern, i.e. the crystals are randomly oriented. (This was independently checked on a Statton camera.) The (111) and (041) peaks are not as sharp as in *Figure 2*, indicating an $\alpha 1$ crystal structure

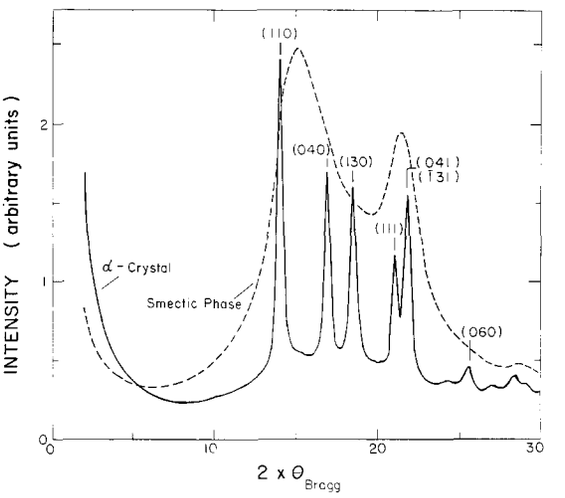

Figure 2 WAXS scans of undeformed, isotropic i-PP in the smectic phase (– – –) and $\alpha 2$ crystal form (——). The first broad peak for the smectic phase is from the interchain packing disorder and the second peak from interchain registration

The 3 × 3 cm square samples cut from the 5.6 mm thick moulded sheet were pre-notched at eight sites to ensure uniform flow during compression. The samples were placed between two 2.5 cm diameter plungers made of hardened tool steel (RC 58/60). The steel plungers were separately heated and controlled within ~ 1°C from the draw temperature (T_{DR}). The latter was determined by placing a thermocouple in the sample. Two highly polished stainless steel plates were used between the plunger and the sample to reduce the friction. The sample and the two plungers were enclosed in a glass wool jacket to ensure isothermal conditions during deformation. The compression load was applied by a Riehel press with a constant ram speed. The compression speeds used in this study were 0.0254 and 0.254 cm min^{-1}. The T_{DR} used were 60 and 140°C. Details of the compression cage and the press were given in an earlier publication[28].

Textural evaluations were carried out on a Siemens D-500 diffractometer with a four-circle Hubber attachment. The X-ray source was CuKα with a nickel filter. The beam was slit collimated with two slits of 0.3° each between the sample and the source and 0.3° and 0.15° slits before the detector. The beam size incident on the sample was $\sim 15 \times 1.5$ mm. The D-500 was interfaced with a PDP 11/34 computer for driving the stepping motors (of the Hubber circle) and for data acquisition and analysis.

A rectangular sample (9.53 × 3.18 mm) was cut from the equibiaxially deformed disc and mounted on a sample holder. The sample was cut such that the longer side of the rectangle was along the θ axis with the shorter side parallel to the r axis. The sample for textural examination was obtained from the area closer to the circumference of the biaxially deformed disc. Since the sample is biaxially oriented, the orientation measurements were performed in both reflection and transmission to measure the complete orientation distribution[35]. Further details of the measurement optics are discussed in the next section with reference to the orientation geometry in *Figure 6*.

RESULTS AND DISCUSSION

To understand the development of crystal textures upon deformation of semicrystalline polymers, it is

essential to determine the shear movements in the crystal at the microscopic level, i.e. the slip system comprising the slip plane and the slip direction. The primary slip plane is usually the strongest-bonded plane, and the primary slip direction is the strongest-bonded direction[36,37]. Since covalent bonding is stronger than the other interchain interactions, the primary slip direction is along the chain axis. This is also referred to as the *c*-slip mechanism[38–41]. To determine the primary slip plane, interchain interactions have to be considered. For example, in polyamides, the plane containing the hydrogen bond will be the primary slip plane. In polymers with no specific interactions (such as i-PP), molecular shape and packing density play major roles in determining the slip planes. For example, in poly(ethylene terephthalate) (PET), the planar chain cross-section causes the primary slip plane to be parallel to the phenyl rings. In polyolefins, where the only interactions between the chains are the van der Waals forces, the plane (containing the chain axis) with the highest density is usually the primary slip plane. Primary slip may preferentially occur along the fold plane in solution-grown single crystals because the adjacent chains are connected in this plane. Martensitic transition, kinking and twining are other important considerations that may relax the stress (and strain) generated from deformation in the crystal[36,42]. However, these mechanisms account for only small amounts of the plastic deformation reported in this study.

On uniaxial compression, the slip plane and slip axis tend to orient perpendicular to the compression direction[37]. Based on the primary slip systems (*hk*0) and $\langle 00l \rangle$, if there is only one major slip plane the texture will be fibre-like, where (*hk*0) corresponding to the slip plane is parallel to the compression axis and $\langle 00l \rangle$ orients randomly about this (fibre) axis. Thus in uniaxial compression, one can determine the complete primary slip system by examining the plane perpendicular to the compression axis.

Figure 3 shows the WAXS patterns for the X-ray beams parallel to the z axis and the θ axis. The area examined is close to the edge of the sample. The pattern in *Figure 3a* was obtained with the beam parallel to the compression axis (i.e. the z axis). Isointensity rings in the pattern signify a random orientation around the compression axis. For the beam incident on the same sample area but along the θ axis, sharp reflections are observed. Thus, i-PP is oriented with a fibre symmetry along the compression axis.

Qualitative observation of the Statton photograph (*Figure 3b*) indicates that the first texture consists of crystals with their chain axes parallel to the r–θ plane. Since all three (*hk*0) reflections (i.e. (110), (040) and (130)) are observed along the z axis (in *Figure 3b*), this suggests that the a and b axes are random around the c axis. The (130) reflection is not clear in the pattern since it is close to the (040) reflection; however, the presence of this reflection will become obvious later in the discussion (in *Figure 5c* there is a pole density maximum at $\alpha = 0°$, which is along the z axis). Furthermore, owing to the cylindrical symmetry about the z axis (*Figure 3a*), the c axis oriented towards the r–θ plane is randomly oriented about the compression axis. This texture is referred to as the planar texture, since the unique axis (the c axis) is oriented with respect to a plane (the r–θ plane). The texture is shown schematically in *Figure 4*.

Two observations from the Statton X-ray pattern (*Figure 3b*) indicate the presence of a second texture: (i)

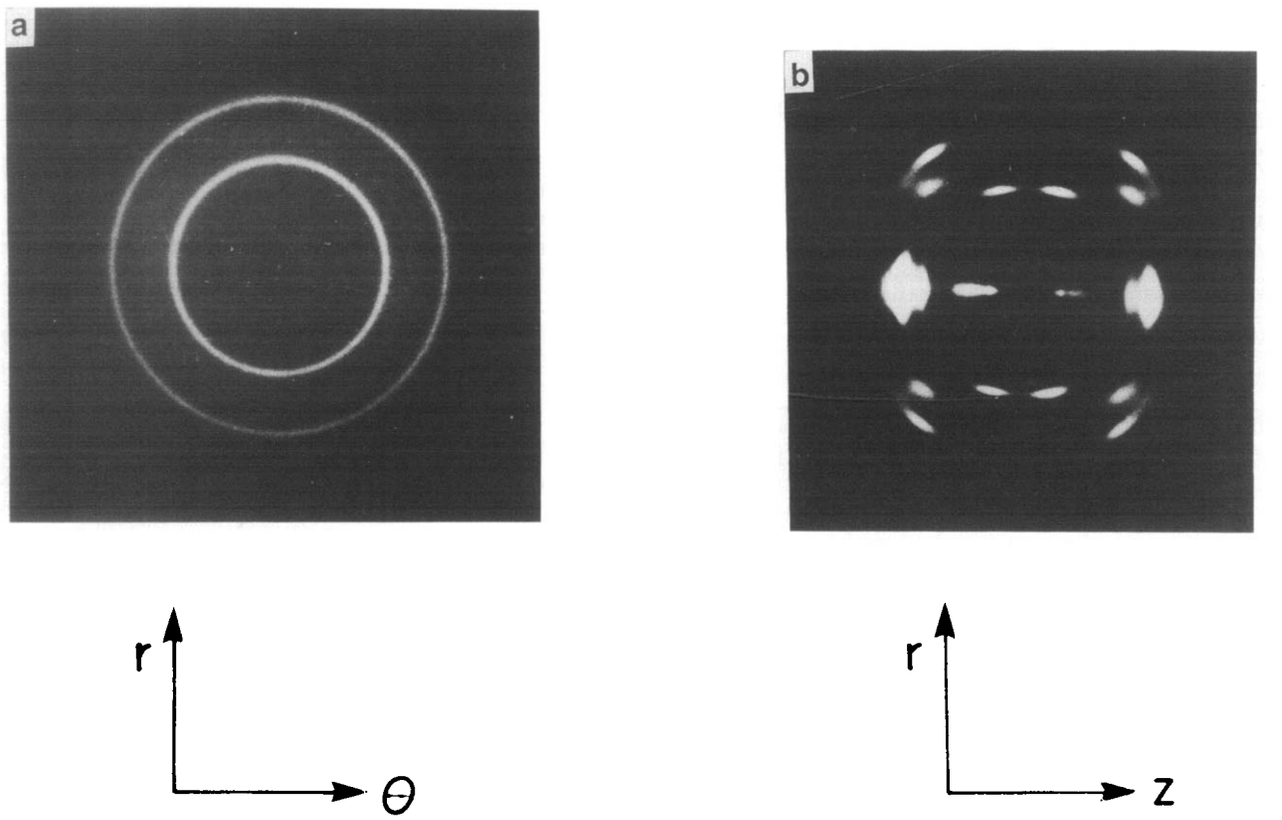

Figure 3 WAXS patterns for the X-ray beam parallel to (a) the z axis and (b) the θ axis. The compression temperature was 140°C and the compression ratio was 24.7 (i.e. biaxial draw of $\sim 5 \times 5$). The compression speed was 0.635 cm min^{-1}

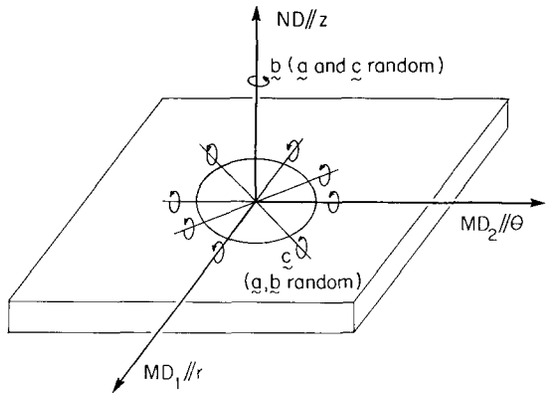

Fiber Texture: b//z (the compression axis)
a, c random around z
a, c//r-θ plane

Planar Texture: c//r-θ plane
c random around z-axis
a, b random around c

Figure 4 Crystal textures of uniaxially compressed i-PP in the solid state. The compression axis is the z axis and the equibiaxially stretched plane is the r–θ plane, with r and θ also denoted by MD_1 and MD_2, respectively

Table 1 Tabulation of the azimuthal angles for the various (*hkl*) reflections on a flat film WAXS pattern for the two textures. The azimuthal angle μ is defined with respect to the z axis (i.e. $\mu=0°$ along the z axis and $\mu=90°$ along the r axis or θ axis in *Figure 3b*). The corresponding azimuthal angles for the intensity maxima based on the two textures may be calculated by a Ewald construction[35]

	Fibre texture			Planar texture		
Reflection (*hkl*)	α_f (°)	ϕ^a (°)	μ^b (°)	α_p (°)	ϕ (°)	μ (°)
(110)	72.5	72.5	72.4	90	0	0
(040)	0	0	0	90	0	0
(130)	46.6	46.6	45.9	90	0	0
(111)	78.5	78.5	43.9	50.3	39.7	43.3
(060)	0	0	0	90	0	0

[a] Latitude of the maximum pole density in *Figure 7*
[b] Azimuthal angle of the (*hkl*) intensity maximum from the equator for a flat film WAXS pattern

both the (110) and (130) have four more spots at 72.4° and 46° from the z axis, respectively; and (ii) the (040) has only two spots along the z axis. The latter suggests that in the second texture the b axis is parallel to the z axis and the a and c axes are randomly oriented around the b axis (because the texture should maintain fibre symmetry, as indicated in *Figure 3a*). For the consistency of this proposed crystal texture with respect to the (110) and (130), the azimuthal locations of the two reflections were calculated for a flat film geometry. *Table 1* indicates the azimuthal angles for the second proposed texture based on the monoclinic unit cell reported by Corrodini and Natta[43]. The measured azimuthal locations are in accordance with the calculated values. This texture is referred to as the fibre texture, since the unique axis (the b axis) is parallel to the axis of cylindrical symmetry.

Since in uniaxial compression the primary slip plane orients perpendicular to the compression axis, the orientation of the (040) plane suggests that the major slip plane is (0k0). Moreover, the strongest direction (the c axis) lies in the (0k0) plane. Thus the primary slip system is composed of (0k0) and ⟨00l⟩. *Figure 4* shows a schematic of both the textures described above. We also note that the azimuthal positions predicted for (111) in *Table 1* for the two textures are consistent with the observations in *Figure 3b*. The actual calculation of their locations is discussed later using *Figure 7* and equation (1). We note that, although the fibre texture corresponding to orientation of the (040) plane perpendicular to the thickness direction is evident in other biaxial deformation processes on i-PP, such as rolling[44,45], rolltrusion[46] and biaxial stretching[47], the planar texture observed here has not been previously reported.

To obtain the pole density distribution function, the measurement of relative intensity for a given (*hkl*) as a function of ϕ was performed. The parameter ϕ is the angle between $\underset{\sim}{\mathbf{R}}(hkl)$ and the z axis (see *Figure 6*). The measurement consists of two parts: a reflection mode and a transmission mode[35]. Briefly, the optics for the two modes are as follows. Let the incident and scattered beams be in the x–y plane such that the momentum vector is parallel to the x axis. In the reflection mode an x scan is performed such that the sample film normal is inclined from $\alpha=0°$ (symmetric condition) to higher values in the x–z plane (see Figure 4-16, ref. 35). In the transmission mode the sample film normal is in the x–y plane but a ϕ scan is performed such that the relative angle between the normal and the momentum vector is changed from $\alpha=90°$ (symmetric condition) to lower values (see Figure 4-13, ref. 35). The tilt angle α (shown in *Figure 5*) for pole density distribution measurement is identical to ϕ. In the reflection and transmission modes tilts from α of 0° to 45° and 90° to 25°, respectively, are performed for measurement. The data are corrected for background, change in path length of the X-ray (i.e. scattering volume) as the sample is tilted, and change in incident flux on tilting the sample[35]. The complete, normalized pole density distribution is obtained by overlapping the corrected data from the reflection and transmission modes in the $\alpha=25°$ to 45° range, as shown in *Figure 5*. *Figure 5* shows the pole density distribution function for i-PP deformed at 60°C to a compression ratio of 14.0 (i.e. the draw ratio in the r–θ plane is 3.74 × 3.74) and annealed at 140°C. Poles (110), (130) and (111) have two maxima and (040) and (060) have only one maximum at 0°. The locations of the maxima are consistent with the values in *Table 1* for the two textures. Thus, the quantitative measurement of the pole density distribution function proves the existence of the double texture.

Figure 6 shows an orientation sphere for a given $\underset{\sim}{\mathbf{R}}(hkl)$ reflection in the reciprocal space. The radius of the sphere is $R=|\underset{\sim}{\mathbf{R}}(hkl)|$. Let $\hat{\mathbf{n}}_i$ be a unit vector parallel to the unique axis. For a planar or fibre texture, $\hat{\mathbf{n}}_i$ is along the c axis (i=p) or b axis (i=f), respectively. Let the orientation of $\hat{\mathbf{n}}_i$ be along QC (as shown in *Figure 6*). The angle between $\hat{\mathbf{n}}_i$ and the X–Y plane is ω. Since the directionality is maintained in the reciprocal to real space transformation, the X, Y and Z axes in the reciprocal space are parallel to the x, y and z axes in real space, respectively. The x–y and r–θ planes are identical and their relative orientations

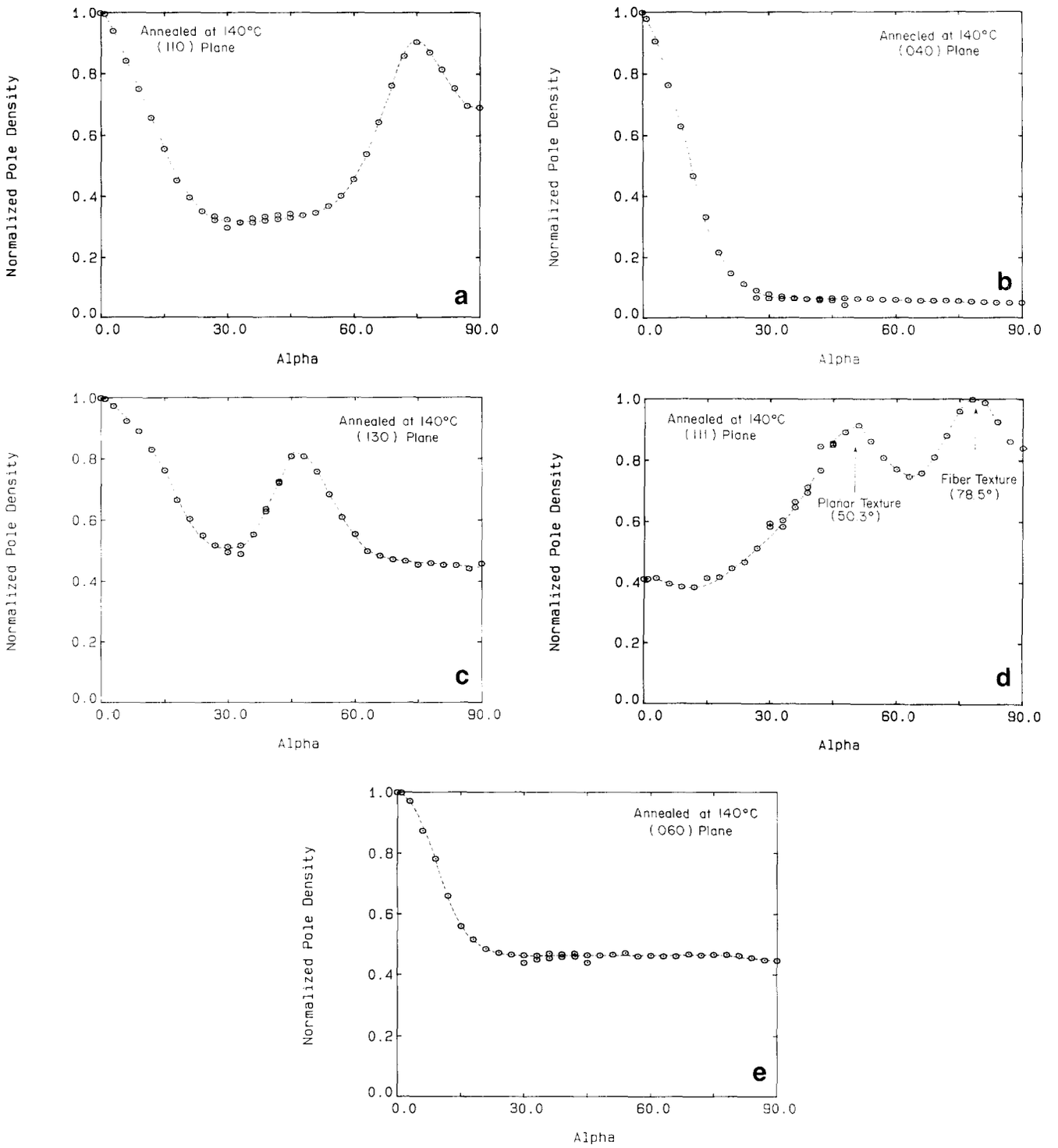

Figure 5 Normalized pole density distributions for i-PP compression drawn at 60°C and annealed at 140°C for 120 min. The compression ratio and speed were 8.03 (i.e. 2.83×2.83) and 0.254 cm min^{-1}, respectively. The reflections for measurement are: (a) (110); (b) (040); (c) (130); (d) (111); (e) (060). The pole density maxima for the planar and fibre textures are in agreement with the calculated angles (*Table 1*)

are arbitrary in the geometry because of cylindrical symmetry about the z axis.

The crystals are randomly oriented around their respective unique axes for both textures. Thus, the texture may be uniquely defined by the orientation distribution function $f_i(\omega)$ of the unique axis. For fibre and planar textures, i = f and p, respectively. For a given $f_i(\omega)$, the pole density distribution function of any $\underset{\sim}{\mathbf{R}}(hkl)$ reflection would be given by[48]

$$\frac{dn(\phi)}{dA} = \frac{f_i(\omega)(\cos\omega)(\sin\alpha_i)}{[\sin(\alpha_i+\omega)-\cos\phi]^{1/2}[\cos\phi+\sin(\alpha_i-\omega)]^{1/2}} \quad (1)$$

where ϕ is the latitude (see *Figure 6*), α_i is the angle between $\hat{\mathbf{n}}_i$ and $\underset{\sim}{\mathbf{R}}(hkl)$, and $dA = R^2 \sin\phi \, d\phi \, d\psi$ is the elemental area on the orientation sphere surface. We note in *Figure 6* that for a planar texture $\hat{\mathbf{n}}_i$ is the c axis, implying that the maximum pole density occurs at $\omega = 0$. Thus, from equation (1), the pole density is a maximum at $\phi = \pi/2 \pm \alpha_p$, where α_p is the angle between the c axis and $\underset{\sim}{\mathbf{R}}(hkl)$. The singularity at these limits is removed when the total pole density is calculated as shown later in equation (2). For a fibre texture, $\hat{\mathbf{n}}_i$ is parallel to the b axis. The maximum pole density in *Figure 6* will occur at $\omega = \pi/2$. Thus the corresponding maximum pole

densities given by equation (1) are at $\phi=\alpha_f$ and $\pi-\alpha_f$, where α_f is the angle between the b axis and $\underset{\sim}{R}(hkl)$.

Figure 7 shows the maximum pole densities for given $\underset{\sim}{R}(hkl)$ corresponding to the two textures. The orientation sphere is in reciprocal space with a diameter equal to $|\underset{\sim}{R}(hkl)|$. The latitude angle ϕ (*Figure 7*) and tilt angle α (*Figure 5*) are identical, since the angles are defined with respect to the Z axis and z axis, respectively, and these are parallel. The rationale for defining the same angle differently is to distinguish between the real space angle (i.e. α) and the reciprocal space angle (i.e. ϕ). Thus the pole density distribution obtained by WAXS as a function of tilt angle should have maxima at $90°-\alpha_p$ and α_f. *Table 1* gives the latitudes for various (hkl) planes. We note here that a cylindrical symmetry is assumed around the unique axes $\hat{\mathbf{n}}_i$ for the two textures. This is indirectly inferred from *Figure 5*. If we did not have such a symmetry, multiple pole density maxima would be observed in *Figure 5*.

The total pole density at a given ϕ is given by integrating over all possible orientations of $\hat{\mathbf{n}}_i(\omega)$ that contribute to the pole density at ϕ. Since $\hat{\mathbf{n}}_i$ has fibre symmetry about the Z axis, no γ dependence (in *Figure 6*) is expected. The total pole density is given by

$$\frac{dN(\phi)}{dA}=\int_{\frac{\pi}{2}-(\alpha_i+\phi)}^{\frac{\pi}{2}+(\alpha_i-\phi)} d\omega \frac{dn}{dA} \tag{2}$$

Since the intensity $I(\phi)$ is proportional to the total number of poles in the solid angle $\Delta\Omega_s(\phi,\psi)=\Delta A_s/R^2$

$$I(\phi)=K\frac{dN(\phi)}{dA}\Delta A_s \tag{3}$$

where $\Delta\Omega_s$ and ΔA_s are respectively the solid angle and the corresponding area (on the orientation sphere) sampled in the WAXS experiment. K is a proportionality constant. The sampling size depends on instrumental parameters, such as beam size and collimation, monochromaticity of the beam, and the intensity detection method. If the scattered intensity is measured on a photographic film, an integrated intensity is measured by modifying ΔA_s (or $\Delta\Omega_s$) further using a Lorentz correction (multiplied by ΔA_s) that depends on the scattered angle and the azimuthal angle α (or ϕ). In the present study, the scattered intensity was measured by a point detector (thus) requiring no Lorentz correction.

In this study, an approximate approach to estimating the relative textures as a function of compression ratio was adopted on the basis of equation (A1) in the Appendix. Let $f_f(\omega)$ and $f_p(\omega)$ be the normalized orientation distribution functions for the b axis (in the fibre texture) and the c axis (in the planar texture), respectively, with respect to the r–θ plane (see *Figure 6*). Since perfect fibre and planar textures would be at $\omega=\pi/2$ and 0, respectively, the approximate fibre to planar ratio may be estimated by $FPR=f_f(\pi/2)/f_p(0)$.

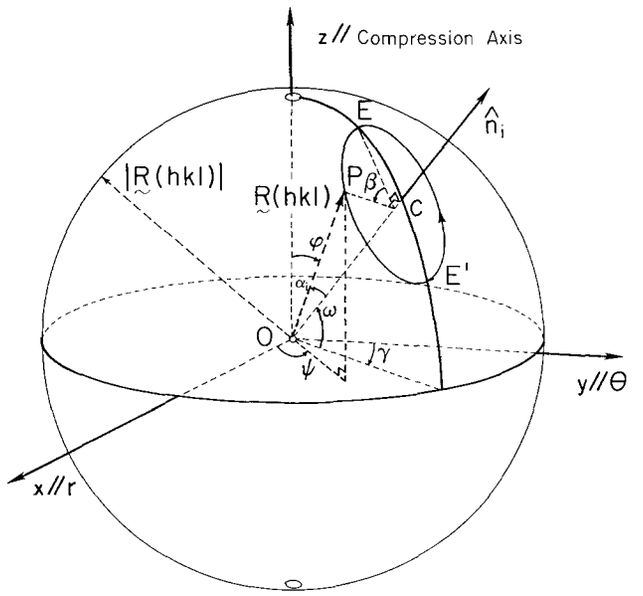

Figure 6 Coordinate axes defining crystal orientation in the reciprocal space (for any (hkl) reflection). The unique axis $\hat{\mathbf{n}}_i$ is defined with respect to angles ω and γ. The $\underset{\sim}{R}(hkl)$ is defined in two ways: (i) with respect to the spherical angles ϕ and ψ; and (ii) with respect to the unique axis by angles β and α_i. The angle α_i between $\hat{\mathbf{n}}_i$ and $\underset{\sim}{R}(hkl)$ is constant for a given reflection. Thus, the angles in representation (ii) (for a given ω) are β and γ

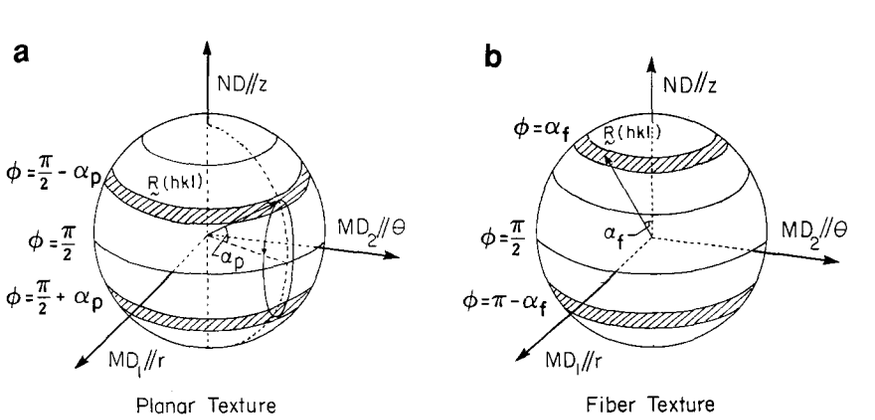

Figure 7 The pole density distributions on an orientation sphere of radius $|\underset{\sim}{R}(hkl)|$. (a) In the planar texture, the c axis orientation along the r–θ plane leads to a family of circles owing to the random orientation of $\underset{\sim}{R}(hkl)$ around the c axis. The latitudes enclosing this family of circles at $\phi=\pi/2\pm\alpha_p$ have the maximum pole density (see equation (1) for $\omega=0$). (b) In the fibre texture, the b axis aligns parallel to the Z axis and $\underset{\sim}{R}(hkl)$ precesses around the b axis. The latitudes for maximum pole density are $\phi=\alpha_f$ and $\pi-\alpha_f$

From the Appendix, for the (110) reflection

$$FPR = \frac{I(\alpha_f)}{I(0)\sin\alpha_f} \quad (4)$$

where α_f is the angle between the vector normal to (110) planes and the b axis. From *Table 1*, $\alpha_f = 72.5°$. As stated in the Appendix, we chose (110) because the pole density maxima for the two textures are well separated (see *Figure 5a*) and the normal to the (110) planes is perpendicular to the c axis.

Equation (4) seems reasonable from simple arguments of fibre symmetry. In the fibre texture, the pole ($hk0$) is spread over the circle $R\sin\alpha_f$ on the orientation sphere. Hence the density is normalized by $1/\sin\alpha_f$. In the case of the planar texture, the pole is concentrated at a point, and hence no normalization factor is required. Dividing the two intensity maxima will give the expression in equation (4). However, items to note are the following: (i) the ratio in equation (4) is approximate, since equation (A3) in the Appendix is approximate; (ii) the contribution from the planar texture is only valid for $\underset{\sim}{\mathbf{R}}(hkl)$ perpendicular to the unique axis; and (iii) the contributions from crystals not in perfect alignment for either of the two textures (i.e. the distribution functions $f_f(\omega)$ and $f_p(\omega)$) are not considered. The shortcoming of equation (4) mentioned in (iii) can be overcome by solving equation (A1) in the Appendix. However, if the functionalities of the orientation distribution functions $f_f(\omega)$ and $f_p(\omega)$ are similar (e.g. if $f_i(\omega)$ is Gaussian), then the ratio of the heights of the two maxima should be a reasonable estimate of *FPR*. This justifies the applicability of equation (4).

The mechanism of the two textures described and experimentally confirmed will now be discussed. The mechanism described predicts (qualitatively) the relative amounts of the two textures as the compression draw increases. The texture development at $T_{DR} = 140°C$ is different from that at $T_{DR} = 60°C$, as shown in *Figures 8* and *9*, respectively, owing to the formation of a smectic phase[49] (i.e. a disordered phase) at $T_{DR} \leqslant 70°C$. We will first discuss the orientation and structural symmetry of the smectic phase. We will then discuss the role of the smectic phase in the texture development of i-PP on deformation and its significance in obtaining the desired structure.

The ratio of the two textures *FPR* is shown in *Figure 8* for i-PP deformed at 140°C. As mentioned

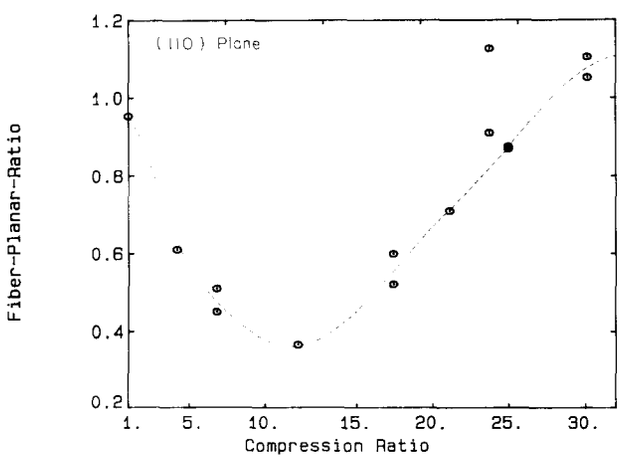

Figure 8 A plot of *FPR versus* compression ratio for i-PP deformed at 140°C at a speed of 0.254 cm min^{-1}. *FPR* is defined in equation (4). The reflection used was (110)

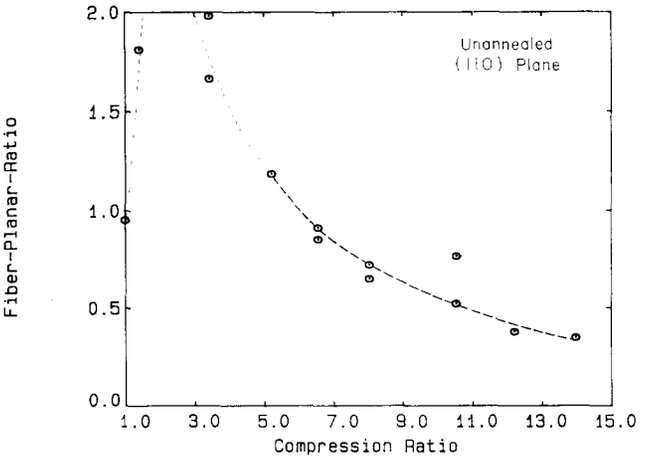

Figure 9 *FPR versus* compression ratio for i-PP deformed at 60°C at a speed of 0.254 cm min^{-1}. The reflection used was (110)

earlier, *FPR* is calculated from the (110) reflection. The compression ratio $CR = 31.15$, corresponding to a biaxial draw ratio of 5.6×5.6, is the highest equibiaxial draw ratio achieved in this study. Since at $CR = 1.0$ the polymer is isotropic, from equation (4) $FPR(CR = 1) = 1.05$. It is obvious from the shape of the curve that at low compression ratios the fibre texture decreases and then increases with compression ratio. The relative amount of the fibre texture increases monotonically and then reaches a plateau at compression ratios higher than 25×. The rationale for this behaviour is discussed next.

The fibre texture, where the b axis (normal to the slip plane) orients along the z axis and the c axis (the slip direction) orients parallel to the r–θ plane with no preferred orientation in the plane, is in accordance with the primary slip system. The planar texture may arise from two possible mechanisms. Firstly, i-PP has more than one ($hk0$) type of slip plane containing the chain axis, analogous to 'pencil glide' in body-centred cubic metals like Fe[37]. Thus the shearing may rotate other ($hk0$) planes perpendicular to the compression axis. Secondly, the orientation is 'incomplete', i.e. the slip direction $\langle 00l \rangle$ rotates in the 'draw plane' but the slip plane does not tilt accordingly. The 'draw plane' is defined by the two draw directions in the biaxial deformation field. For uniaxial compression the r–θ plane is the draw plane. The first mechanism, suggesting a number of ($hk0$)-type slip planes, will predict no fibre texture. Since this is contrary to the result observed, the first mechanism may not be a dominant factor leading to the planar texture. Now consider the second mechanism. In *Figure 10* let P be a slip plane ($h''k''l''$) ((0k0) for i-PP) containing the slip direction $\underset{\sim}{\mathbf{D}}(\omega, \psi)$. The slip plane is at an angle δ with respect to plane P′, where P′ is a plane at an angle ω to the draw plane r–θ (i.e. the normal to P′ makes an angle ω with the z axis). (Note that the angles in *Figure 10* correspond to the angles in *Figure 6*, where the chain axis is the slip direction $\underset{\sim}{\mathbf{D}}$.) A compressive force along the z axis induces a shear stress in the slip plane P. This initiates a rotation of the slip direction $\underset{\sim}{\mathbf{D}}$ towards the r–θ plane, i.e. ω is reduced as the deformation progresses. To reduce further the shear stress on plane P, δ should also decrease. The second step, involving the rotation about the slip direction $\underset{\sim}{\mathbf{D}}$, may occur if: (i) there is a secondary slip direction in the slip plane P at an angle to $\underset{\sim}{\mathbf{D}}$; and/or (ii) owing to local heterogeneity the resultant lines of compressive force on the two sides of the slip plane are not collinear[49]. This will generate a torque on

the crystal that will 'force' the slip plane parallel to the r–θ plane. If the shear force is not adequate to cause either of the two processes, δ will be (almost) unchanged as the deformation progresses, inducing orientation of $\underset{\sim}{D}$ but no orientation of the slip plane. Thus, only the planar orientation will exist, i.e. *FPR* (equation (4)) will decrease monotonically with compression ratio. *Figure 8* indicates that at low draw ratios the process is 'incomplete'. However, *FPR* increases monotonically after a compression ratio above ~12, indicating orientation of the primary slip plane (0k0) parallel to the r–θ plane. Although not pursued in this study, in principle the coupled rotation of ω and δ in *Figure 10* can be determined from the pole inversion formula in equation (4) applied to the pole distributions of (110), (040) and (111) as a function of compression ratio for the planar and fibre textures (i.e. $f_i(\omega)=f_f(\omega)$ and $f_p(\omega)$).

Figure 11 shows diffractometer scans along and perpendicular to the z axis for a sample deformed at 60°C. The scan along the z axis was obtained in the symmetric transmission condition, i.e. for $\alpha=90°$. The scan perpendicular to the z axis was obtained in the symmetric reflection condition, i.e. for $\alpha=0°$. The (110) and (040) reflections overlap in the scan along the z axis (i.e. reflection mode). This is due to the formation of a smectic phase, which has a broad reflection between (110) and (040), as shown in *Figure 2*. That the (110) and (040) peaks do not overlap in the scan perpendicular to the z axis (i.e. transmission mode) indicates that the smectic phase is oriented parallel to the r–θ plane. The (110) and (040) reflections sharpen and separate after annealing at 140°C, as shown in *Figure 12*. This is because the smectic phase transforms to the crystal[49] on annealing above 70°C. The (110) and (040) peaks in the unannealed sample for the transmission scan (*Figure 11*) do not overlap. This indicates that the first broad smectic peak (*Figure 2*) is along the z axis. Since the first WAXS peak for the smectic phase is due to the interchain packing[33–50], the chains of the smectic phase are oriented parallel to the r–θ plane, implying that the smectic phase has a planar texture. This is not surprising since the interchain packing of the 3/1 helices in the smectic phase is liquid-like[33–50]. As the amount of smectic phase increases with deformation[49], the apparent planar texture content increases with *CR*. This implies that the texture ratio *FPR* will decrease with *CR*, consistent with the observation in *Figure 9*. Thus the monotonic decay of *FPR* with *CR* at $T_{DR}=60°C$, in contrast to 140°C (*Figure 8*), is due to the smectic phase formation.

Owing to the 'cylindrical symmetry' of the smectic phase about the chain axis[33], on annealing at 140°C the α crystal formed should have the c axis parallel to the chain axis of the smectic phase, but the a and b axes will orient randomly about the c axis. Therefore, the texture after annealing should be more planar than fibre-like. *Figure 13* shows a normalized pole density distribution for the (110) reflection of i-PP deformed at 60°C and subsequently annealed at 140°C for 120 min. The observation is contrary to the above argument. The shape of the peak around $\alpha=0°$ (corresponding to the planar texture) is constant, but the peak at $\alpha=72.5°$ increases significantly after annealing. This indicates that the α crystal formed from the smectic phase is (close to 100%) fibre-like in orientation.

The fibre texture of the annealed smectic phase may be explained by considering the deformation mechanism of i-PP in the solid state. The smectic phase may form by two mechanisms from the crystal present in the initial,

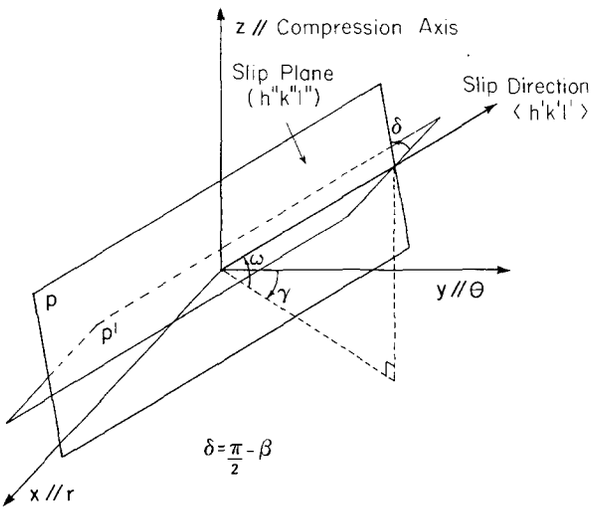

Figure 10 The movement of slip plane P at an angle δ with respect to the reference plane P'. The plane P' is at angles ω and γ with respect to the x–y plane. On compression, the slip direction $\underset{\sim}{D}$ orients along the x–y plane at an angle γ with respect to the y axis. The slip plane tends towards the x–y plane but δ may not completely reduce to zero

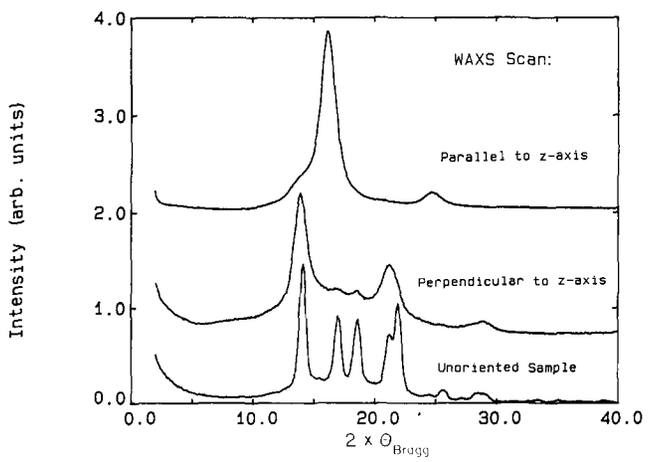

Figure 11 WAXS scans for i-PP deformed to a compression ratio of ~3 × 3 at 60°C and a speed of 0.0254 cm min^{-1}. The (110) and (040) reflections are broad and overlap for the scan along the z axis. The two reflections are separate for the scan perpendicular to the z axis. The scan for an isotropic (as-moulded sample) is given for reference

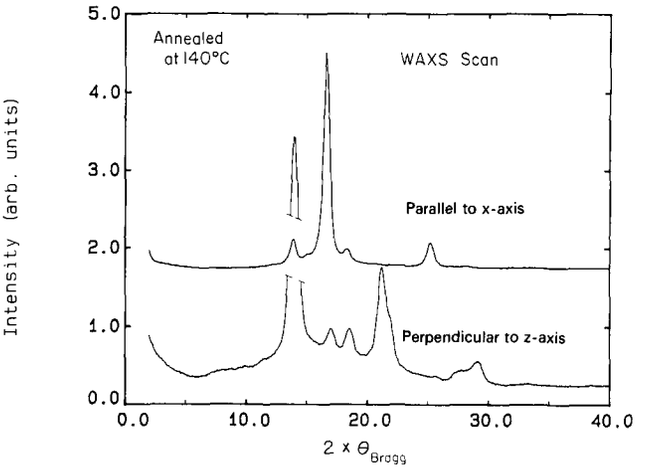

Figure 12 WAXS scans for the sample in *Figure 11* after annealing for 120 min at 140°C. Note that the (110) and (040) reflections sharpen and separate after annealing

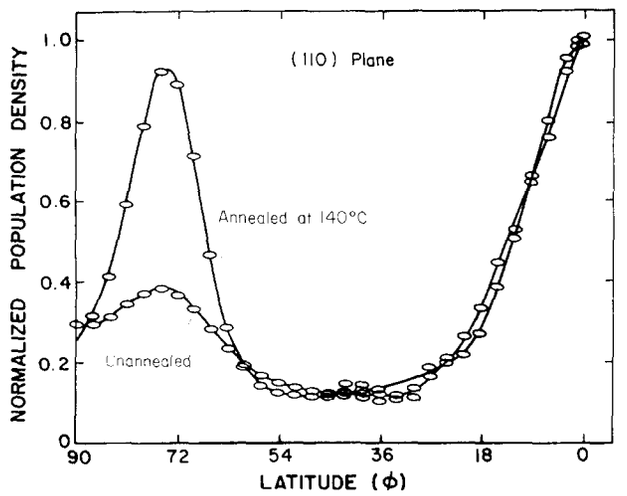

Figure 13 Effect of annealing on the normalized pole density distribution. There is a large increase in the fibre texture on annealing i-PP deformed at 60°C (draw ratio 3.75 × 3.75). The planar texture density is almost unchanged

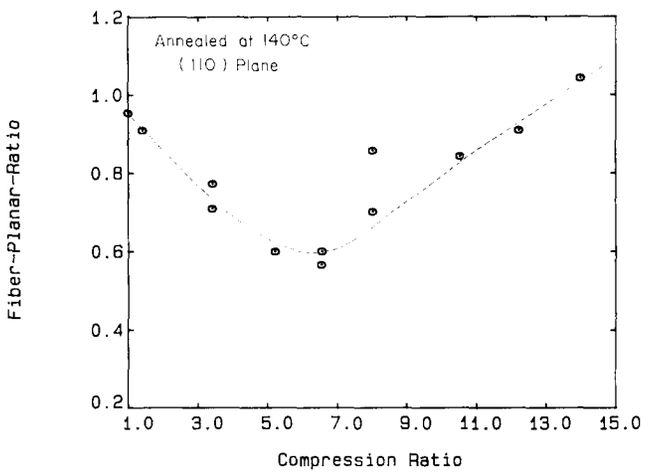

Figure 14 *FPR versus* compression ratio after annealing (at 140°C for 120 min) the i-PP compression drawn at 60°C (compression speed 0.254 cm min^{-1}). The trend of the curve is similar to that in *Figure 8*

undeformed i-PP[49].

1. The smectic phase can form by a lateral packing disorder process caused by surface forces. In this mechanism, the lamellar fragment between the shear planes transforms to the smectic phase owing to a high surface to volume ratio.
2. The smectic phase can form by recrystallization of the pulled out chains from the crystal parallel to the shear plane. Since the pulled out chains maintain their conformation the process may be referred to as 'decrystallization'.

In either case, the *c* axis (i.e. the chain axis) of the smectic phase will be closely aligned to the slip plane (0*k*0) of the mother crystal. Thus, on annealing, the smectic phase will crystallize on the (0*k*0) surface of the parent crystal from which it originated. Since the (0*k*0) tends to orient parallel to the r–θ plane, the resultant crystal (formed from the recrystallization of the smectic phase) will lead to a fibre texture.

Figure 14 shows the ratios of the textures obtained for i-PP deformed at 60°C and annealed at 140°C for 120 min. Comparison of *Figure 14* with *Figure 8* indicates that the fibre texture content is much higher in the samples that deform via the order–disorder transition. Since the fibre texture is the desired orientation where the slip plane is parallel to the draw plane, the order–disorder transition enhances the crystal orientation process on deformation.

SUMMARY

This study has demonstrated the planar and fibrillar texturing that occurs on equibiaxial deformation of semicrystalline polymers. A method of quantifying the relative amounts of the two textures was presented. The pole density formula equation (A1) may be used to quantify texture development in other semicrystalline polymers and crystalline materials with uniaxial symmetry. The quantitative demonstration of pole density maxima at $\phi = \pi/2 \pm \alpha_p$ for the planar texture has not, to our knowledge, been previously presented in a closed form. The following are the salient conclusions on uniaxially compressed i-PP.

1. The major slip systems for deformation of i-PP are (0*k*0) and ⟨00*l*⟩.
2. There are two textures induced by uniaxial compression, namely the planar texture and the fibre texture.
3. For deformation at 140°C (where no stable smectic phase is produced during deformation), the relative amount of the planar texture increases with the compression ratio.
4. For deformation at 60°C (where the smectic phase forms due to deformation), an apparent increase in the planar texture is observed. However, on transforming the smectic phase to the crystal (by annealing at 140°C), the behaviour is similar to that in 3.
5. The smectic phase seems to form by lamellae unravelling at the (0*k*0) slip plane.
6. The relative amount of the fibre texture is higher if i-PP is deformed via the order–disorder process at 60°C and annealed at 140°C, rather than by deformation only at 140°C.

ACKNOWLEDGEMENT

I would like to thank Professor Roger S. Porter of University of Massachusetts for his critical comments, insightful discussions, and constant encouragement on this study.

REFERENCES

1 Ward, I. M. (Ed.) 'Structure and Properties of Oriented Polymers', Wiley, New York, 1975
2 Zachariades, A. E. and Porter, R. S. (Eds) 'The Strength and Stiffness of Polymers', Marcel Dekker, New York, 1983
3 Peterlin, A. *J. Mater. Sci.* 1971, **6**, 490
4 Imada, K., Yamamoto, T., Shigematsu, K. and Takayanagi, M. *J. Mater. Sci.* 1971, **6**, 537
5 Mead, W. T., Zachariades, A. E., Shimada, T. and Porter, R. S. *Macromolecules* 1979, **12**, 473
6 Zachariades, A. E., Mead, W. T. and Porter, R. S. *Chem. Rev.* 1980, **80**, 351
7 Hadziioannou, G., Wang, L.-H., Stein, R. S. and Porter, R. S. *Macromolecules* 1982, **15**, 880
8 Glenz, W., Morosoff, N. and Peterlin, A. *Polym. Lett.* 1971, **9**, 211
9 Speerchneider, C. J. and Li, C. H. *J. Appl. Polym. Sci.* 1962, **33**, 1871
10 Kojima, M. *J. Polym. Sci., Polym. Phys. Edn* 1967, **5**, 567
11 Ingram, I. and Peterlin, A. *J. Polym. Sci. B* 1964, **2**, 736
12 Kiho, H., Peterlin, A. and Geil, P. H. *J. Polym. Sci. B* 1965, **3**, 257

13 Morrow, D. R. and Woodward, A. E. *J. Macromol. Sci., Phys. B* 1970, **4**, 153
14 Klement, J. J. and Geil, P. H. *J. Macromol. Sci., Phys. B* 1972, **6**, 31
15 Shultz, J. M. and Petermann, J. *Colloid Polym. Sci.* 1984, **262**, 294
16 Gohil, R. M. and Petermann, J. *J. Polym. Sci., Polym. Phys. Edn* 1979, **17**, 525
17 Petermann, J., Klug, W. and Gleiter, H. *J. Polym. Sci., Polym. Phys. Edn* 1979, **17**, 1043
18 Kanig, G. *J. Cryst. Growth* 1980, **48**, 303
19 Yang, D. C. and Thomas, E. L. *J. Mater. Sci.* 1984, **19**, 2098
20 Adams, W. W., Yang, D. C. and Thomas, E. L. *J. Mater. Sci.* 1986, **21**, 2239
21 Zachariades, A. E. and Porter, R. S. (Eds) 'The Strength and Stiffness of Polymers', Marcel Dekker, New York, 1983, p. 1
22 Kanamoto, T., Tsuruta, A., Tanaka, K., Takeda, M. and Porter, R. S. *Macromolecules* 1988, **21**, 470
23 Kanamoto, T., Tsuruta, A., Tanaka, K. and Takeda, M. *Polym. J.* 1984, **16**, 75
24 Sakurada, I., Ito, T. and Nakamae, K. *J. Polym. Sci. C* 1966, **15**, 75
25 DeVries, A. J. *Polym. Eng. Sci.* 1983, **23**, 241
26 Shimomura, Y., Spruiell, J. E. and White, J. L. *J. Appl. Polym. Sci.* 1982, **27**, 2663
27 DeVries, A. J., Bonnebat, C. and Beautemps, J. *J. Polym. Sci. C* 1977, **58**, 109
28 Saraf, R. F. and Porter, R. S. *J. Rheol.* 1987, **31**, 59
29 Guam, J. Y., Saraf, R. F. and Porter, R. S. *J. Appl. Polym. Sci.* 1987, **33**, 1517
30 Zannetti, R., Celotti, G., Fichera, A. and Francesconi, R. *Makromol. Chem.* 1969, **128**, 137
31 Wyckoff, H. W. *J. Polym. Sci.* 1962, **62**, 83
32 Nakamura, K., Imada, K. and Takayanagi, M. *Polymer* 1974, **15**, 446
33 Saraf, R. F. and Porter, R. S. *Mol. Cryst. Liq. Cryst. Lett.* 1985, **2**, 85
34 Guerra, G., Petraccone, V., Corradini, P., De Rosa, C., Napolitano, R. and Pirozzi, B. *J. Polym. Sci., Polym. Phys. Edn* 1984, **22**, 1029
35 Alexander, L. E. 'X-ray Diffraction Methods in Polymer Science', Wiley, New York, 1969, reprinted by Krieger, Huntington, NY, 1979
36 Hirth, J. P. and Lothe, J. 'Theory of Dislocations', 2nd Edn, McGraw-Hill, New York, 1982
37 Honeycombe, R. W. K. 'The Plastic Deformation Of Metals', 2nd Edn, Edward Arnold, Baltimore, 1984
38 Zaukelis, D. A. *J. Appl. Phys.* 1961, **33**, 2797
39 Kurokawa, M. and Ban, T. *J. Appl. Polym. Sci.* 1964, **8**, 971
40 Keller, A. and Rider, J. G. *J. Mater. Sci.* 1966, **1**, 389
41 Peterlin, A. *J. Mater. Sci.* 1971, **6**, 490
42 Bassett, D. C. 'Principles of Polymer Morphology', Cambridge University Press, Cambridge, 1981, p. 229
43 Natta, G. and Corrodini, P. *Nuovo Cimento Suppl.* 1960, **15**, 40
44 Wilchinsky, Z. W. *J. Appl. Polym. Sci.* 1963, **7**, 923
45 Dhingra, V. J., Spruiell, J. E. and Clark, E. S. *Polym. Eng. Sci.* 1981, **21**, 1063
46 Shanker Narayanan, M. J. and Magill, J. H. *J. Mater. Sci.* 1986, **21**, 267
47 Hinrichsen, G., Eberhardt, A., Lippe, U. and Springer, H. *Colloid Polym. Sci.* 1981, **259**, 73
48 Saraf, R. F. *Macromolecules* 1988, **21**, 2382
49 Saraf, R. F. and Porter, R. S. *Polym. Eng. Sci.* 1988, **28**, 842
50 Corradini, P., Petraccone, V., De Rosa, C. and Guerra, G. *Macromolecules* 1986, **19**, 2699
51 Saraf, R. F., Lefebvre, J. M., Porter, R. S. and Wignall, G. D. *Mater. Res. Soc. Symp. Proc.* 1987, **79**, 263

APPENDIX: CALCULATION OF FIBRE TO PLANAR RATIO (*FPR*)

Substituting equation (2) into equation (3) with the proper limits yields

$$I(\phi)=K\Delta A_s\int_{\frac{\pi}{2}-(\alpha_i+\phi)}^{\frac{\pi}{2}+(\alpha_i-\phi)} \times d\omega \frac{f_i(\omega)(\cos\omega)(\sin\alpha_i)}{[\sin\omega-\cos(\alpha_i+\phi)]^{1/2}[\cos(\alpha_i-\phi)-\sin\omega]^{1/2}} \quad \text{(A1)}$$

Equation (A1) is a Voltera integral of the I kind, where $I(\phi)$ is known and $f_i(\omega)$ is to be determined. The equation can be solved numerically[51] to obtain $f_i(\omega)$. Thus, for a random orientation around the unique axis and fibre symmetry about the z axis, equation (A1) prescribes a method to determine experimentally the orientation distribution function of the unique axis.

Consider the fibre texture first. For a perfect fibre texture $\hat{\mathbf{n}}_i=\hat{\mathbf{n}}_f$ is along the Z axis, i.e. $\omega=\pi/2$. Equation (A1) gives

$$\frac{dn(\phi)}{dA}=\begin{cases}0 & \phi\neq\alpha_f\\ f_f(\pi/2) & \phi=\alpha_f\end{cases} \quad \text{(A2)}$$

If the contributions from $\hat{\mathbf{n}}_f$ (i.e. the b axis) oriented at other ω values (i.e. off the Z axis) to the pole density at ϕ are neglected, equations (2), (3) and (A2) give

$$I_f(\phi=\alpha_f)=Kf_f(\pi/2)R^2(\sin\alpha_f)\Delta\phi_s\Delta\psi_s \quad \text{(A3)}$$

where $I_f(\phi)$ is the intensity distribution of the fibre texture. Note that equation (A3) is an approximation. The exact relation would be given by equation (A1) as

$$I_f(\phi=\alpha_f)=K\Delta A_s\int_{\frac{\pi}{2}-2\alpha_f}^{\frac{\pi}{2}} d\omega \frac{f_f(\omega)(\cos\omega)(\sin\alpha_f)}{(\sin\omega-\cos 2\alpha_f)^{1/2}(1-\cos\omega)^{1/2}} \quad \text{(A4)}$$

Consider the planar texture next. For a perfect planar texture $\hat{\mathbf{n}}_i=\hat{\mathbf{n}}_p$ is parallel to the X–Y plane, i.e. $\omega=0$. It is possible to calculate $f_p(\phi=0)$ exactly for $\mathbf{R}(hkl)$ perpendicular to $\hat{\mathbf{n}}_p$. This is obtained as follows. For $\alpha_p=\pi/2$, equation (1) becomes

$$\frac{dn}{dA}(\phi)=\frac{f_p(\omega)\cos\omega}{(\cos\omega-\cos\phi)^{1/2}(\cos\omega+\cos\phi)^{1/2}} \quad \text{(A5)}$$

For $\omega=0$, equation (A5) reduces to

$$\left[\frac{dn}{dA}(\phi)\right]_{\omega=0}=\frac{f_p(0)}{(1-\cos^2\phi)^{1/2}}=\frac{f_p(0)}{\sin\phi} \quad \text{(A6)}$$

Furthermore, only $\hat{\mathbf{n}}_p$ along the X–Y plane contributes to the pole density at the orientation sphere pole ($\phi=0$). Therefore

$$\frac{dn}{dA}(\phi=0)=\frac{dN}{dA}(\phi=0) \qquad \alpha_p=\frac{\pi}{2} \quad \text{(A7)}$$

Substituting equations (A6) and (A7) into equation (3) yields

$$I_p(\phi=0)=K\frac{f_p(0)}{\sin\phi}R^2(\sin\phi)\Delta\phi_s\Delta\psi_s$$

$$\Rightarrow I_p(\phi=0)=Kf_p(0)R^2\Delta\phi_s\Delta\psi_s \quad \text{(A8)}$$

where $I_p(\phi)$ is the intensity distribution of the planar texture.

Thus, the fibre to planar ratio *FPR* can be obtained by dividing equation (A3) by equation (A8) and rearranging to give

$$\frac{I_f(\alpha_f)}{I_p(0)}=\frac{f_f(\pi/2)\sin\alpha_f}{f_p(0)} \quad \text{(A9)}$$

where α_f is the angle between the vector normal to the ($hk0$) planes and the b axis. Since the pole density maxima due to the two textures for the (110) reflection are well separated (as is evident in *Figure 5*), $I_p(0)\approx I(0)$ and $I_f(\alpha_f)\approx I(\alpha_f)$. Thus, equation (A9) becomes

$$FPR=\frac{f_f(\pi/2)}{f_p(0)}=\frac{I(\alpha_f)}{I(0)\sin\alpha_f} \quad \text{(A10)}$$